Constraints on the time-scale of nuclear breakup from thermal hard-photon emission

R. Ortega[1,2a], D. d'Enterria[1,2,3b], G. Martínez[2,3], D. Baiborodin[4], H. Delagrange[2,3], J. Díaz[5], F. Fernández[1], H. Löhner[6], T. Matulewicz[7], R.W. Ostendorf[6], S. Schadmand[8], Y. Schutz[2,3c], P. Tlusty[4], R. Turrisi[3d], V. Wagner[4], H.W. Wilschut[6], and N. Yahlali[5]

[1] Grup de Física de les Radiacions, Universitat Autònoma de Barcelona 08193, Catalonia
[2] SUBATECH, 4, rue Alfred Kastler BP20722 44307 Nantes Cedex 3, France
[3] GANIL, Grand Accélérateur National d'Ions Lourds, IN2P3-CNRS, DSM-CEA, 14076 Caen Cedex 5, France
[4] Institute of Nuclear Physics, 20568 Řež, Czech Republic
[5] Institut de Física Corpuscular, Universitat de Valencia-CSIC, Dr Moliner 50, 46100 Burjassot, Spain
[6] Kernfysisch Versneller Instituut, 9747 AA Groningen, The Netherlands
[7] Institut of Experimental Physics, Warsaw University, 00681 Warsaw, Poland
[8] Institut für Kernphysik, Forschungszentrum Jülich, D-52457 Jülich, Germany

Abstract. Measured hard photon multiplicities from second-chance nucleon-nucleon collisions are used in combination with a kinetic thermal model, to estimate the break-up times of excited nuclear systems produced in nucleus-nucleus reactions at intermediate energies. The obtained nuclear break-up time for the ^{129}Xe + ^{nat}Sn reaction at $50A$ MeV is $\Delta\tau \approx 100 - 300$ fm/c for all reaction centralities. The lifetime of the radiating sources produced in seven other different heavy-ion reactions studied by the TAPS experiment are consistent with $\Delta\tau \approx 100$ fm/c, such relatively long thermal photon emission times do not support the interpretation of nuclear breakup as due to a fast spinodal process for the heavy nuclear systems studied.

PACS. 21.65.+f – 25.70.-z – 13.75.Cs – 64.70.Dv

1 Introduction

Nucleus-nucleus collisions are the only available tool to explore in the laboratory the different domains of the nuclear phase diagram. In heavy-ion (HI) collisions at intermediate energies (bombarding energies between $20A$ MeV and $100A$ MeV) the projectile and target traverse each other in a time scale $t \lesssim 50$ fm/c forming a compressed and excited transient system that usually disassembles into several intermediate-mass-fragments (IMF) in a process known as "nuclear multifragmentation" [1]. The exact physical mechanism that drives this breakup is up to date an open issue. Two opposite scenarios have been considered: a fast breakup from an expanding source, consistent with a spontaneous spinodal mechanism, and a sequential slower breakup from a thermally equilibrated source. The knowledge of the relative importance of these

two mechanisms is essential to find-out a possible connection between nuclear multifragmentation and the occurrence of a "liquid-gas"-like phase transition [2] in nuclear systems with excitation energies in the range $\epsilon^\star = (3-8)A$ MeV, where a flattening of the "caloric curve", signaling a possible liquid-gas phase transition, has been observed [3, 4,5,6]. To discern between both possible mechanisms it is necessary to establish the breakup time of the multifragmenting system.

The experimental observable used in the present analysis in order to probe the thermodynamical state of the produced transient nuclear systems, and in particular, to delimit the nuclear breakup time is thermal hard photon emission. At intermediate-energy HI collisions, photons above 30 MeV (hard photons) issue from bremsstrahlung in incoherent proton-neutron collisions [7]. The main hard photon contribution, the so-called "direct" component, is emitted from first-chance nucleon-nucleon (NN) collisions in the preequilibrium stage of the reaction. A second and softer flash of hard photons is emitted from secondary NN collisions in the later stages [8,9] from a thermalizing source [10]. Hence, the experimental hard photon spectrum measured in HI reactions has been found to be well reproduced by the sum of two exponential distributions

[a] *Present address: Physikalisches Institut, Universität Heidelberg, Philosophenweg 12 D-69120 Heidelberg, Germany*
[b] *Present address: Nevis Laboratories, Columbia University 538 W. 120th St. NY 10027, USA*
[c] *Present address: CERN, CH-1211 Genève, Switzerland*
[d] *Present address: INFN-Padova, Via Marzolo 8, 35131 Padova, Italy*

[9]:

$$\frac{d\sigma}{dE_\gamma} = K_d\, e^{-E_\gamma/E_0^d} + K_t\, e^{-E_\gamma/E_0^t} \qquad (1)$$

where d and t stand for direct and thermal, respectively, and the factors $K_{d,t}$ are related to the intensity of each source. The power of first chance bremsstrahlung photons is the fact that they result from incoherent collisions. This allowed one to equate the observed intensity and slope of the gamma spectrum with the number and hardness of collisions respectively. With the kinematic thermal model [11] this information can also be obtained from secondary collisions; the soft spectrum now corresponds to the number of collisions integrated over the lifetime of the equilibrated source and its formation, and the slope parameter is related to the average temperature of the source [12]. Although multiple collisions lead to bremsstrahlung quenching (see e.g. [13]) it is believed not to play an important role because we exploit the photon spectrum above $E_{\gamma cut}$=30 MeV. To observe about 10% quenching the collision rate of the nucleons in the thermal source should not exceed $E_{\gamma cut}$/hbar=$1.5 \cdot 10^{-1}$ (fm/c)$^{-1}$, in the model, without considering Pauli blocking, the rate typically is $1.3 \cdot 10^{-1}$ (fm/c)$^{-1}$. Thus the time scales derived in this work are not limited by the quenching phenomena.

The analysis presented in this paper has two different goals. First, we want to elucidate the dependence of the thermal photon temperature on the reaction centrality in ^{129}Xe + ^{nat}Sn reactions at $50A$ MeV; at this energy, this heavy and symmetric system provides good conditions for observing the effects of a possible nuclear liquid-gas phase transition, and moreover, the charged-particle distributions and related observables have been studied in detail for this reaction by the INDRA Collaboration (see e.g.[14, 15,16,17,18] and references therein). The second objective consists in assessing the nuclear breakup time-scales using the measured second-chance photon multiplicities and a thermal model that describes well the observed spectra. This investigation is performed for 7 different reactions studied by the TAPS Collaboration: ^{86}Kr + ^{58}Ni at $60A$ MeV [8], ^{181}Ta + ^{197}Au at $40A$ MeV [8], ^{208}Pb + ^{197}Au at $30A$ MeV [8], ^{36}Ar + ^{107}Ag at $60A$ MeV [10], ^{36}Ar + ^{197}Au at $60A$ MeV [10], ^{36}Ar + ^{58}Ni at $60A$ MeV [10] and ^{129}Xe + ^{nat}Sn at $50A$ MeV. The paper is organized as follows: in Sect. 2 the experimental setup is described. In Sect. 3 the particle identification methods are presented. The results obtained from the analysis of the inclusive hard photon spectrum are summarized in Sect. 4. In Sect. 5 we focus on the $Xe + {}^{nat}$Sn exclusive measurements; first, we present the experimental centrality classes as well as the method employed to estimate the average impact parameter; next, we present the direct and thermal hard photon measurements for each centrality class. In Sect. 6, the thermodynamical properties extracted from the thermal hard photon signal are presented. In particular in 6.2 the results on the lifetimes of the thermal hard photon sources obtained for the different reactions are presented. Section 7 gives a summary.

2 Experimental setup

The experiment E-300 was performed at the "Grand Accélérateur National d'Ions Lourds" (GANIL) located in Caen, France, during 13 days of total beam time in May 1998. The GANIL accelerator system delivered a Xe^{46+} beam of $50A$ MeV with a bunch rate of 10 MHz and a nominal intensity of 5 nA, around 68 ions per pulse. The Xe ions impinged on a ^{nat}Sn target of 1 mg/cm^2 thickness (with associated interaction probability of $1.9 \cdot 10^{-3}$ per burst). The experimental setup consisted of the "Two Arms Photon Spectrometer" TAPS associated with three particle multidetectors: the GANIL Silicon Strip Detector (SSD), the Washington University "Dwarf Ball" (DB) and the KVI "Forward Wall" (FW). A general layout of the experimental setup is presented in Fig. 1.

The TAPS electromagnetic calorimeter [19] consists of 384 scintillation modules. Each one consisted of a BaF$_2$ hexagonal crystal, 2.95 cm inner radius and 25 cm length (corresponding to $12X_0$ radiation lengths) [20,21], and a Charged Particle Veto (CPV) detector of plastic (NE102A) scintillator. TAPS offers a large solid angle coverage allowing for high quality angular distribution measurements in a wide energy range, from statistical (E$_\gamma$> 5 MeV) to the hardest photons (E$_\gamma \approx$ 200 MeV). In this experiment TAPS modules were arranged in six blocks of 64 modules (8×8), which were placed in an almost symmetrical configuration in the horizontal plane around the target, and at an average distance of 56 cm, covering about 20% of the full solid angle.

The GANIL silicon strip detector telescope SSD was placed at 19 cm downstream the target inside the vacuum chamber, covering the angular range of $2.2° \leq \theta \leq 10.3°$. This device, consisting of a first disk 150 μm thick with 64 semicircular strips and of a second disk 500 μm thick with 128 radial strips, was sensitive to projectile-like fragments (PLF) emitted in binary reactions and intermediate-mass fragments (IMF) emitted in the forward direction from more dissipative reactions.

The Washington University "Dwarf Ball" (DB) [22] covered an angular range of $31° \leq \theta \leq 168°$ around the target. This detector system allows to identify light-charged particles (LCP) and IMF. The Dwarf Ball (DB) consists of 64 phoswich detectors forming a sphere with an inner radius of 41.5 mm. Each phoswich detector is made of a thin plastic scintillator and of a CsI(Tl) inorganic crystal scintillator. The plastic scintillator type (Bicron BC400 or BC446) depends on the covered angle and so does its thickness, 10 μm and 40 μm for the most backward and forward modules, respectively. The CsI(Tl) crystal glued on the back of each plastic is 4 mm to 8 mm thick, depending also on the angle.

The KVI "Forward Wall"(FW) [23], consisted of 92 plastic scintillator phoswiches, detects and identifies LCP and IMF (up to Z$\approx$15) emitted in the forward direction. In our experimental setup, this detector was placed downstream 74 cm away from the target covering the forward hemisphere behind the SSD, $2.5° \leq \theta \leq 25°$ and the whole azimuthal range. Each FW phoswich is composed of two organic plastic scintillators which are heat-pressed
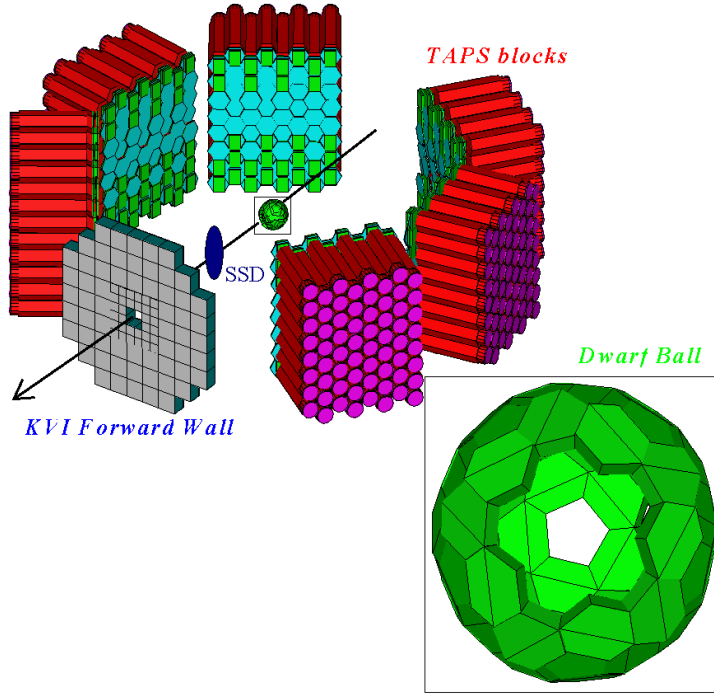
Fig. 1. *General layout of the experimental setup used to study the reaction $^{129}Xe+^{nat}Sn$ at 50A MeV at GANIL. The detector system consists of the Silicon Strip Detector (SSD), the Washington University Dwarf Ball (DB), the TAPS electromagnetic calorimeter and the KVI Forward Wall (FW).*

together; a 1 mm thick "fast" ($\tau = 2.4$ ns) NE102A plastic followed by a 50 mm thick "slow" ($\tau = 320$ ns) NE115 plastic.

This complete experimental setup allowed correlated measurements of photons and charged-particles, necessary to study the dependence of the hard-photon production on the reaction topology. The photon data were recorded with the minimum bias trigger for neutral particles (γ*DB), which signaled events with at least one neutral hit in TAPS of energy $E_\gamma > 10$ MeV detected in coincidence with one or more charged particles in the Dwarf Ball. The minimum bias (MB) reaction trigger was defined by the condition of detecting at least a charged particle in the Dwarf Ball.

3 Particle identification

Photons are identified in TAPS by means of a Pulse Shape (PSA) vs. time-of-flight (TOF) analysis and the CPV information. Photons and leptons induce a stronger intensity of the fast BaF_2 light component compared to hadronic particles, producing therefore a higher ratio of the fast to the slow energy components in the BaF_2 (PSA). Photons and relativistic electrons are located in time within a prompt peak centered at TOF=1.87 ns (with a resolution $\sigma = 340$ ps [24]); these particles produce hence a recognizable contour in the PSA-TOF spectrum. In order to separate photons from relativistic electrons the information (fired or not) delivered by the CPV of each module is used. Nevertheless, given that cosmic muons have mainly vertical trajectories not firing the CPV, and have random TOF, they can be misidentified as photons. This is avoided by defining a PSA-TOF cosmic contour several nanoseconds far from the photon contour but with the same dimensions. Subsequently, the energy and angular spectra measured within this contour (see Fig. 2) are subtracted from the raw photon energy and angular spectra respectively.

The ΔE - E telescope technique [24, 25] allows the charge identification of LCP and IMF detected in the DB and in the FW, as well as of the PLF and IMF impinging on the SSD. The light measured in the first stage of each multi-detector (the first component of each phoswich in the DB and the FW, or the first disk in the SSD) and the signal of the second component are plotted in bidimensional histograms in which the different curves correspond to different Z. In the DB, additional LCP isotopic identification was also possible exploiting the pulse shape properties of the CsI(Tl) light.

4 Inclusive hard photon spectra in ^{129}Xe + ^{nat}Sn at 50A MeV reactions

Figure 2 shows the inclusive raw photon energy spectrum measured in the ^{129}Xe + ^{nat}Sn reaction from the collection
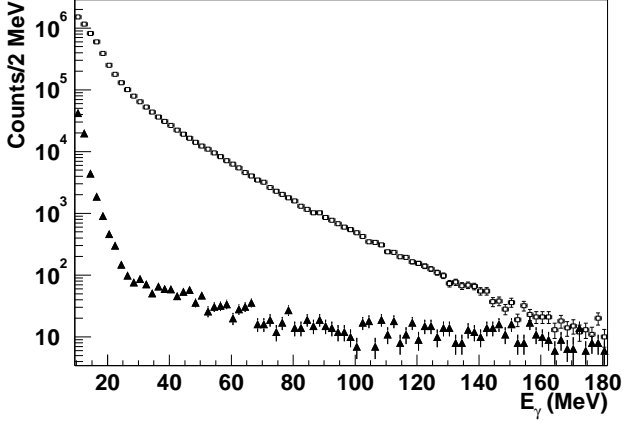
Fig. 2. *Inclusive raw photon spectrum measured in the center-of-mass frame for the reaction $^{129}Xe + ^{nat}Sn$ at 50A MeV. The triangles show the cosmic ray background contribution.*

Table 1. *Summary of the experimental inclusive hard photon ($E_\gamma > 30$ MeV) results obtained for the $^{129}Xe + ^{nat}Sn$ reaction at 50A MeV. For the direct and thermal γ components we quote: inverse slope E_0, relative intensity I, source velocity β, cross-section σ_γ, multiplicity M_γ, and (only for the direct component) hard photon probability P_γ.*

	Direct	Thermal
E_0(MeV)	15.6 ± 1.0	7.0 ± 0.6
I (%)	78 ± 1	22 ± 1
β	0.15 ± 0.01	0.16 ± 0.01
σ_γ(mb)	4.9 ± 0.6	1.4 ± 0.2
M_γ	$(9.3 \pm 0.8) \cdot 10^{-4}$	$(2.6 \pm 0.3) \cdot 10^{-4}$
P_γ	$(7.8 \pm 0.7) \cdot 10^{-5}$	-

of $5.8 \cdot 10^6$ photons with $E_\gamma > 10$ MeV detected in TAPS and transformed into the CM frame ($\beta_{AA} \approx \beta_{NN} \approx 0.15$). After cosmic-ray subtraction, and for energies $E_\gamma > 30$ MeV this spectrum is well described by the double source fit of Eq. 1 (Fig. 3). The direct component exhibits an inverse slope parameter $E_0^d = (15.6 \pm 1.0)$ MeV whereas the thermal slope parameter is $E_0^t = (7.0 \pm 0.6)$ MeV. Both slopes are in agreement with the direct [26] and thermal [12] photon slope systematics measured in intermediate $A + A$ reactions. Thermal hard photons account for 22% of the total yield above 30 MeV. The strength and intensity of the thermal emission are also confirmed by a double source analysis of the hard photon angular distribution; however, due to the symmetry of the system, the NN and AA source velocities cannot be disentangled [27].

The direct (thermal) hard photon multiplicity, i.e. the number of direct (thermal) hard photons emitted per nuclear reaction, has been obtained via the following expression:

$$M_\gamma^i = \frac{\sigma_\gamma^i}{\sigma_R} \quad (2)$$

where i stands for direct or thermal, σ_γ^i is the experimental hard photon cross section determined by integrating the corresponding $d\sigma/dE_\gamma$ spectrum above $E_\gamma = 30$ MeV, and $\sigma_R = (5300 \pm 600)$ mb is the experimental total reaction cross section for Xe+Sn, obtained from the charged particle distribution measured in the DB with the MB reaction trigger. We report the direct and thermal hard photon cross sections and multiplicities in Table 1. The direct hard photon probability P_γ^d, i.e. the probability to produce a hard photon in a first-chance proton-neutron collision, is determined from the experimental direct hard photon multiplicity:

$$P_\gamma^d = \frac{\sigma_\gamma^d}{\sigma_R \cdot \langle N_{pn} \rangle_b} = \frac{M_\gamma^d}{\langle N_{pn} \rangle_b} \quad (3)$$

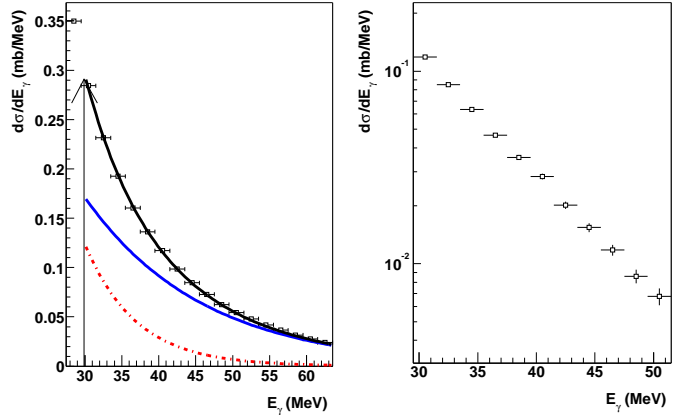**Fig. 3.** *Left panel: experimental inclusive hard photon spectrum measured for the reaction $^{129}Xe + ^{nat}Sn$ at 50A in the range $E_\gamma = 30$ - 65 MeV, fitted to the Eq. 1, the solid (dashed) line is the direct (thermal) exponential distribution. Right panel: inclusive thermal hard photon spectrum obtained after subtracting the fitted direct component.*

where $\langle N_{pn} \rangle_b$ is the number of first chance pn collisions averaged over impact parameter, calculated from the geometrical "equal-participant" model of Nifenecker and Bondorf [28]. $\langle N_{pn} \rangle_b$ is = 11.79 for the Xe on Sn system. The measured P_γ^d in $^{129}Xe + ^{nat}Sn$ reactions at 50A MeV is $(7.8 \pm 0.7) \cdot 10^{-5}$. We note that we do not quote a thermal hard photon probability, since we should determine the average number of secondary (and not primary) pn collisions, from which the thermal component originates, and this number is not well determined experimentally nor theoretically. More details of the inclusive analysis can be found in [24].

Table 2. *Conditions on the fragment multiplicity in the SSD (M^{SSD}), the charged particle multiplicity (IMF + LCP) in the DB (M^{DB}) and the FW (M^{FW}) that define each centrality class. The contribution to the reaction cross-section, and to the nuclear reactions detected by the minimum bias photon trigger (γ*DB) for each centrality class are reported.*

Centrality class	Multiplicity condition	$\%\sigma_R$	$\%\sigma_R(\gamma\text{*DB})$
A or Periph.	$M^{DB+FW} = 1\text{-}2$ and M^{SSD} ($\theta < 5$) $= 0$	57%	23%
B	$M^{DB+FW} = 1\text{-}2$	67%	26%
C	$2 < M^{DB+FW} < 8$	38%	58%
D	$5 < M^{DB+FW} < 9$	10%	24%
E	$6 < M^{DB+FW} < 10$	7%	18%
F or Central	$9 < M^{DB+FW} < 15$	2%	6%

Table 3. *Characteristics of the six centrality classes considered for Xe+Sn reactions at 50A MeV. For each centrality bin we quote: average charged particle multiplicity M_{cp} and impact parameter $\langle b \rangle_{geo}$ estimated with the geometrical model of Cavata et al. [29]; direct photon multiplicity (M_γ^d), average number of first chance proton-neutron collisions $\langle N_{pn} \rangle$ obtained as described in [30,31], and associated averaged impact parameter $\langle b \rangle_\gamma$ estimated using the "equal-participant" model [28].*

Centrality class	$\langle M_{cp} \rangle$	$\langle b \rangle_{geo}$ (fm)	M_γ^d	$\langle N_{pn} \rangle$	$\langle b \rangle_\gamma$ (fm)
A or Periph.	1.5	9.4 ± 0.8	$(3.2 \pm 0.2)\cdot10^{-4}$	4.1 ± 0.6	9.2 ± 0.3
B	1.5	9.4 ± 0.8	$(4.1 \pm 0.3)\cdot10^{-4}$	5.2 ± 0.6	8.8 ± 0.3
C	4.7	5.2 ± 0.4	$(1.5 \pm 0.1)\cdot10^{-3}$	18.6 ± 2.2	5.9 ± 0.5
D	6.8	3.3 ± 0.3	$(2.4 \pm 0.2)\cdot10^{-3}$	30.7 ± 3.7	4.0 ± 0.6
E	7.8	2.6 ± 0.2	$(2.8 \pm 0.2)\cdot10^{-3}$	36.1 ± 4.4	3.1 ± 0.7
F or Central	11.4	0.9 ± 0.1	$(3.8 \pm 0.4)\cdot10^{-3}$	48.9 ± 6.7	1.3 ± 1.1

5 Exclusive hard photon analysis in ^{129}Xe + ^{nat}Sn at 50A MeV reactions

5.1 Selection of centrality classes

Six centrality classes of ^{129}Xe + ^{nat}Sn collisions have been selected to investigate the dependence of the thermal hard photon production on the reaction centrality. This choice results from a compromise between requiring a wide impact parameter coverage and obtaining enough hard photon statistics for each centrality class. We report in Table 2 the conditions on the fragment multiplicities measured in the SSD, Dwarf Ball and Forward Wall that define the selected centrality bins.

5.2 Estimation of the impact parameter for minimum bias data

In order to estimate the impact parameter b in ^{129}Xe + ^{nat}Sn all reactions, recorded by means of the MB trigger, we apply the geometrical method proposed by Cavata *et al.* [29], which relies on the monotonous decrease of M_{CP} as a function of b. An alternative method to estimate the impact parameter in experiments where hard photon emission can be analyzed is based on the correlation of the direct hard γ yield with the impact parameter [30,31]. In this method, for a given reaction class, the experimental average number of first chance *pn* collisions $\langle N_{pn} \rangle$ is estimated, making use of Eq. 3, from the experimentally

measured M_γ^d and from the P_γ^d, which is considered to depend only on the Coulomb corrected bombarding energy. The obtained $\langle N_{pn} \rangle$ values are related to the impact parameter b by the geometrical "equal-participant" model of of Nifenecker and Bondorf [28]. We note that if the impact parameter is obtained directly from the total hard photon yield, as commonly done, instead of only from the direct component, the deduced impact parameter might be distorted for reactions where a thermal photon contribution cannot be neglected. The average impact parameter for each reaction class, obtained by means of the direct hard photon multiplicities and by means of the charged particle multiplicities measured in the DB, are reported in Table 3. We find a good agreement between both methods, and in addition the whole impact parameter range is covered.

5.3 Determination of the impact parameter for reactions where a hard photon is produced

We want to exploit the properties of the thermal hard photon component as a tool to extract the thermodynamical state of the radiating source. It is therefore of crucial importance to determine as accurately as possible any bias introduced in the estimation of the impact parameter for particular reactions where a hard photon is produced.

Within a given centrality class, defined by a range in the M_{cp} distribution, hard photons are mostly emitted in reactions with high M_{cp} values, characterized by a large projectile-target overlap, and consequently by a high number of *pn* collisions. This bias through lower impact pa-

rameters can be reproduced by the geometrical "equal-participant" model; the reaction cross-section as a function of b for reactions where a hard photon is produced, $\sigma_R^\gamma(b)$, is modulated by the product of $\sigma_R(b)$ and $N_{pn}(b)$. As a consequence, the ratio between the reaction cross-section $\sigma_R^\gamma(b)$ and the total (integrated over b) σ_R^γ is a representable function sensitive to the cross section deviation through lower b (see Fig. 4). It is thus possible to estimate the average impact parameter for reactions where a hard photon is produced by means of an extension of the geometrical model of Cavata *et al.*, correlating the experimental $\sigma_R^\gamma(M_{cp})/\sigma_R^\gamma$ and the theoretical $\sigma_R^\gamma(b, N_{pn})/\sigma_R$ obtained from the geometrical "equal-participant" model. The average b of each centrality class has been obtained with this method after weighting the b(M_{cp}) by the contribution of each M_{cp} within the centrality class. Table 4 reports the $\langle b \rangle$ estimated for each RC for reactions where a hard γ is emitted.

Table 4. *Estimated average impact parameter $\langle b \rangle$ for each of the six centrality classes considered.*

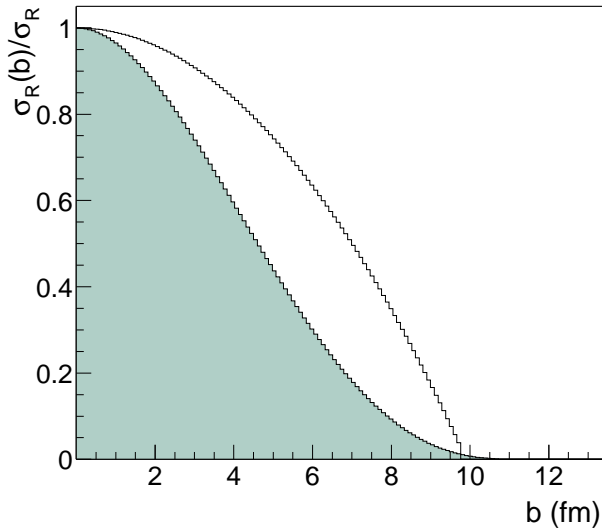| Centrality class	$\langle b \rangle_{geo}$ (fm)
Class A or Peripheral	7.6 ± 0.3
Class B	7.2 ± 0.3
Class C	4.2 ± 0.4
Class D	2.8 ± 0.4
Class E	2.2 ± 0.6
Class F or Central	1.0 ± 0.9

Fig. 4. *Evolution of $\sigma_R(b)/\sigma_R$ as a function of the impact parameter without (empty histogram) and with (filled histogram) the condition that a hard photon is produced.*

5.4 Centrality dependence of the hard photon production

The two-exponential fit of Eq. 1 reproduces the hard photon energy spectrum of each one of the six centrality classes, from peripheral to central events. The corresponding direct and thermal slopes parameters and intensities are listed in Table 5. Whereas the measured $E_0^t(b)$ differ by up to 24% from the inclusive value, the direct slope variation amounts to less than 5% of the inclusive E_0^d. The measurement of an almost constant direct slope confirms that the E_0^d is an observable that depends just on the bombarding energy [9]. Only for very peripheral reactions it is expected to observe a decrease of the direct photon slope mainly due to the decrease of the Fermi momentum in the surface of the nucleus [31]. In Fig. 5 the values of the thermal (direct) slopes are displayed as a function of the thermal (direct) multiplicities. The direct hard photon slope is independent of the direct hard photon multiplicity. This shows that the increase of the direct hard γ multiplicity with the centrality is just a consequence of the associated increase of the number of first-chance pn collisions. On the other hand, the thermal slope exhibits a linear dependence on the thermal multiplicity. This trend, observed for the first time, indicates that, assuming that the size of the thermalized source remains almost constant with centrality, the thermal production is sensitive to the excitation of the nuclear system. This result is supported by the inclusive thermal systematics collected by the TAPS Collaboration: the thermal slopes and thermal multiplicities divided by the size of the system, scale with the energy available in the nucleus-nucleus center-of-mass [10,24].

5.5 Exclusive analysis of the GDR emission

Exploiting the wide dynamic range of TAPS, we have estimated the γ yield from the Giant Dipole Resonance (GDR) decay emitted in peripheral ^{129}Xe + ^{nat}Sn reactions. The main motivation of this investigation was to identify a possible thermal bremsstrahlung and GDR mixture in the low energy range ($E_\gamma \approx 30$ MeV) of the hard photon spectra, which could distort the measurement of the thermal hard photon yield. Peripheral reactions exhibit the highest probability of GDRγ contamination because the reached excitation energies can still be not high enough for suppression of the collective mechanisms responsible of the GDRγ emission [34], and because of the softer observed thermal emission. So the GDR analysis in peripheral reactions allowed us to conclude about a possible GDRγ contamination for all reaction classes.

In order to perform the GDRγ analysis, the direct and thermal hard photon components have been subtracted from the total photon spectra. This subtraction is done by extrapolating the double hard γ exponential fit down to the lowest energy, given by the TAPS LED threshold of 10 MeV. This extrapolation technique is routinely applied in GDR measurements from HI reactions (see *e.g.* [32,33,34]).

Table 5. *Characteristics of the hard photon spectra measured in the six different centrality classes: direct (E_0^d) and thermal (E_0^t) slopes, ratio of thermal to total hard-photon intensities (I_t/I_{tot}), and thermal photon multiplicity (M_γ^t).*

Centrality class	E_0^d (MeV)	E_0^t (MeV)	I_t/I_{tot}(%)	M_γ^t	χ^2/ndf
A or Periph.	14.9 ± 0.9	5.7 ± 0.5	19 ± 1	$(7.6 \pm 0.7)\cdot10^{-5}$	1.5
B	14.6 ± 0.9	5.7 ± 0.5	19 ± 1	$(8.9 \pm 1.1)\cdot10^{-5}$	1.2
C	15.6 ± 0.9	6.3 ± 0.6	19 ± 1	$(3.4 \pm 0.4)\cdot10^{-4}$	1.0
D	16.0 ± 1.0	7.8 ± 0.7	25 ± 1	$(7.8 \pm 0.6)\cdot10^{-4}$	1.4
E	16.1 ± 1.1	7.9 ± 0.7	25 ± 1	$(9.4 \pm 0.6)\cdot10^{-4}$	1.2
F or Central	15.9 ± 1.0	8.7 ± 0.8	27 ± 2	$(1.4 \, ^{+0.2}_{-0.3})\cdot10^{-3}$	1.0
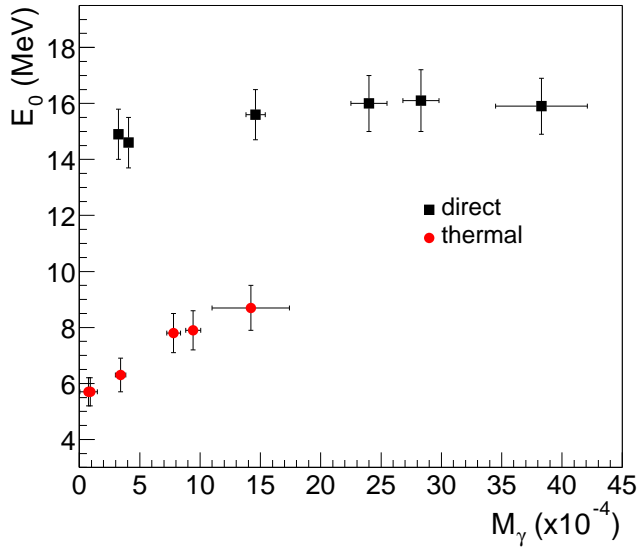
Fig. 5. *Direct and thermal hard photon slopes vs their respective multiplicities for the six Xe+Sn centrality classes considered.*

We have compared the GDR spectra measured for peripheral centrality classes A and B with the GDR distributions measured with the multidetector MEDEA and reported by T. Suomijärvi *et al.* [34]. In this work, the GDRγ emission from hot nuclei of A $\approx$ 115 formed in the ^{36}Ar + ^{90}Zr at $27A$ MeV reaction is investigated in detail. The comparison of the GDRγ yield measured in this analysis and the one measured for peripheral reactions in our work comes easily to mind when considering the similarities in mass and in excitation energy of the emitting sources:

– In peripheral ^{129}Xe + ^{nat}Sn reactions the quasi-projectile and quasi-target are close to the ^{129}Xe and ^{nat}Sn masses. Assuming that both, quasi-target and quasi-projectile, develop collective GDR oscillations after the collision, the photon spectrum measured in the peripheral centralities scaled by a factor of $\sim$1/2 can be compared to the GDR γ yield emitted by a nuclei of A $\sim$ 115;

– In spite of the different geometry and bombarding energy of both reactions, the excitation energies reached at large impact parameters in ^{129}Xe + ^{nat}Sn reactions ($\sim 3A$ MeV, see next section) are comparable with the $\epsilon^\star$ attained in the ^{36}Ar + ^{90}Zr MeV reaction at $27A$. Besides, the GDR yield measured for the ^{36}Ar + ^{90}Zr system has been found to remain constant with the excitation energy [34] (see Fig. 6).
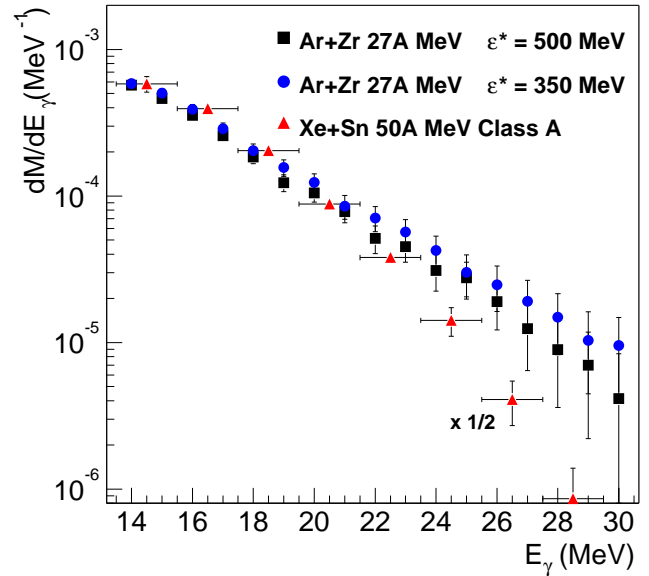
Fig. 6. *Spectra in the GDR region for the ^{36}Ar + ^{90}Zr reaction [34], for two different excitation energies: $\epsilon^\star = 350$ MeV (dots), $\epsilon^\star = 500$ MeV (squares)[34], compared to the experimental γ spectrum obtained in peripheral ^{129}Xe + ^{nat}Sn reactions (triangles) after subtraction of the hard-photon yield (extrapolated down to 10 MeV).*

The GDR yields (the γ spectra after subtraction of the bremsstrahlung contribution) for the ^{36}Ar + ^{90}Zr reaction for $\epsilon^\star = 350$ MeV and for $\epsilon^\star = 500$ MeV from [34], and the GDR yield estimated for the ^{129}Xe + ^{nat}Sn centrality class

A[1] are plotted together in Fig. 6. The global compatibility of the three distributions assures the validity of the estimation of the GDR yield for the peripheral Xe+Sn hard photon spectra. The difference found in the 25-30 MeV region between the TAPS and MEDEA measurements is due to the fact that in the latter the subtracted hard photon distribution is parameterized by a single exponential. Taking into account that for peripheral reactions the total photon multiplicity is around $9 \cdot 10^{-5}$ at $E_\gamma = 30$ MeV and that the GDR yield at this energy is found to be lower than 10^{-5} (see Fig. 6), we conclude that the GDR contamination in the low energy range of the hard photon spectra can be neglected. This result is in good agreement with the highest energy GDR gamma contribution predicted from the systematics. Indeed, taking the centroid energy of the GDR as $E_{GDR} = 76.5 A^{-1/3}$ and the maximum width $\Gamma_{GDR} \approx 12$ MeV [34,35], the GDR emission neither from the Xe projectile nor from the Sn target are expected to exceed 28 MeV.

6 Derived (thermo)dynamical properties

6.1 Nuclear Temperature

Although, due to their long mean free path in nuclear matter, thermal hard photons are not in thermal equilibrium with the source, their spectral shape is directly correlated to the temperature of the radiating nuclear fragment. As in our previous analyses [12], we use the kinetic thermal model of Neuhauser and Koonin [11] to calculate the relation between the inverse slope E_0^t and the temperature T of the nuclear system. The electromagnetic radiation rate emitted by a hot and equilibrated nuclear fragment is expressed in this model as a function of the local density and temperature of the source. It is assumed that bremsstrahlung in proton-neutron collisions is the main source of thermal photon emission for $E_\gamma > 30$ MeV. The hard photon spectra thus calculated are accurately approximated by an exponential with slope E_0^t in agreement with the experimental data [12]. The evolution of E_0^t values extracted from a fit above 30 MeV with the temperature, T, is quantitatively well described by the following linear expression:

$$T(\text{MeV}) = (0.78 \pm 0.02) \cdot E_0^t(\text{MeV}) \quad (4)$$

in the region T $\approx 3\text{-}10$ MeV and $\rho \approx (0.3\text{-}1.2)\rho_0$ [12]. We have applied this photon thermometer to extract the temperature of the radiating system produced in the different ^{129}Xe + ^{nat}Sn centralities studied in this work. The obtained temperatures are reported in Table 6. The temperature of the nuclear system for central collisions (centrality class F, $b/b_{max} \leq 0.1$) is a 50% $\pm$ 20% higher than for peripheral collisions (centrality class A, $b/b_{max} \approx 0.6$).

---

[1] the GDR yield measured for centrality classes A and B are almost identical, so only the yield for class A is shown in the figure.

Table 6. *Nuclear temperatures T estimated through Eq. 4 from the experimental thermal hard photon slopes E_0^t of the inclusive and exclusive hard photon spectra measured in $^{129}Xe + {}^{nat}Sn$ at 50A MeV.*

Centrality class	E_0^t (MeV)	T (MeV)
Inclusive	7.0 ± 0.6	5.5 ± 0.8
A or Peripheral	5.7 ± 0.5	4.4 ± 0.4
B	5.7 ± 0.5	4.4 ± 0.4
C	6.3 ± 0.6	4.9 ± 0.5
D	7.8 ± 0.7	6.1 ± 0.5
E	7.9 ± 0.7	6.2 ± 0.5
F or Central	8.7 ± 0.8	6.8 ± 0.6

6.2 Lifetime of the thermalized system

The multiplicity of hard photons emitted by an equilibrated nuclear fragment can be calculated by means of the model of Neuhauser and Koonin from the following expression [12]:

$$M_\gamma^{NK} = \int d^3x \int dt \int_{30}^\infty \frac{dR_\gamma^{NK}(T,\rho)}{dE_\gamma} dE_\gamma \quad (5)$$

where $R_\gamma^{NK}(T,\rho)$ is the rate of photons emitted from a thermal nuclear fragment with temperature T and density ρ. From this model, $R_\gamma^{NK}(T,\rho)$ is found to scale with $\sim T^{6.7}$ and to be proportional to ρ. The quadratic dependence of the photon rate on ρ expected naively turns out to be linear due to the Pauli blocking. The photon rate can be hence expressed as $R_\gamma^{NK} \approx R_0^{NK} \cdot T^{6.7} \cdot \rho$, with the constant $R_0^{NK} = 1.1 \cdot 10^{-13}$ MeV$^{-6.7} \cdot$(fm/c)$^{-1}$. We can further simplify Eq. 5, by assuming that the temperature is uniform in the volume V and roughly constant during the emission time,

$$M_\gamma^{NK} \approx V \cdot \Delta\tau \cdot R_0^{NK} \cdot T^{6.7} \cdot \rho \quad (6)$$

where V and $\Delta\tau$ are respectively the volume and the lifetime of the radiating nuclear source. The volume can be approximated as the ratio of the sum and the projectile and target nucleons [2] over the nuclear density, $V \approx (A_t + A_p)/\rho$.

With these simplifying assumptions, the thermal hard photon yield, scaled to the relative size of the system, can be written as:

$$\frac{M_\gamma^{NK}}{(A_t + A_p)} \approx \Delta\tau \cdot R_0^{NK} \cdot T^{6.7} \quad (7)$$

This relation, which is independent of the density, can be exploited to estimate the lifetime $\Delta\tau$ of the thermal equilibrated source, by fitting Eq. (7) to the experimentally measured multiplicities (reported in Table 5) as a function

---

[2] We neglect here emission of particles during preequilibrium.

of the temperature. Figure 7 shows the experimental (inclusive) M_γ^t, divided by size of the system $A_{tot} = A_t + A_p$, as a function of the estimated T, for the Xe+Sn and the six other reactions studied [12]. The lines correspond to the calculated M_γ^{NK} as a function of the T for two different lifetimes ($\Delta\tau=100$ fm/c and $\Delta\tau=35$ fm/c).

The calculated multiplicities successfully reproduce the experimental thermal hard photon yields measured for all the reactions (see Figs. 7 and 8), with $\Delta\tau$ values about 100 fm/c, which are consistent with the expected lifetime of an equilibrated source (see e.g. [36]). This result con-
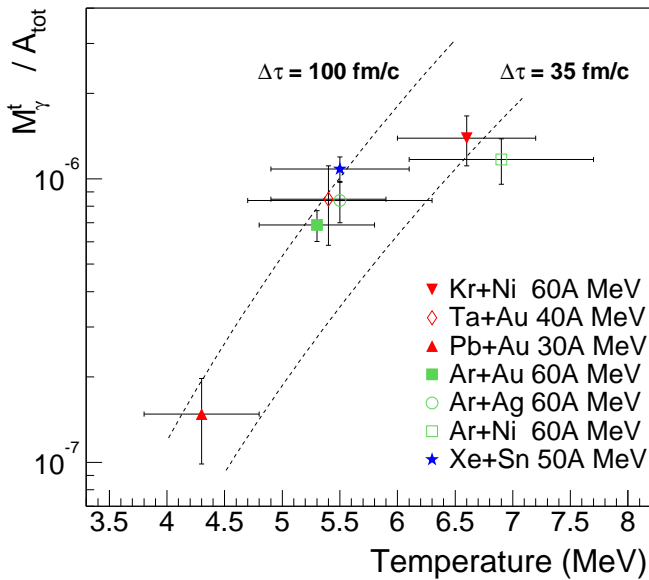

Fig. 7. *Experimental thermal bremsstrahlung multiplicity, M_γ^t, divided by the size of the colliding system, $A_{tot} = A_t + A_p$, plotted as a function of the extracted nuclear temperatures, for the different reactions studied by the TAPS Collaboration. The lines correspond to two different values of the source lifetime estimated with Eq. 7.*

firms the validity of the thermal model, since it reproduces both experimental observables, the slope of the thermal hard photon spectrum and the thermal multiplicity, with the temperature as the single input parameter. In Figs. 7 and 8, it can be observed that all the systems studied have a lifetime $\Delta\tau$ of the order or larger than 100 fm/c, except the two lighter systems at 60A MeV, ^{86}Kr+^{58}Ni and ^{36}Ar+^{58}Ni, which seem to survive a shorter $\Delta\tau \sim 35$ fm/c, similar to the transit time of the colliding ions. In these two reactions, the achieved excitation energy is also higher than in the rest of reactions [12]. This difference in $\Delta\tau$ might indicate that equilibrated nuclear sources break faster when they have a smaller size or higher excitation energies, as observed in [36,37,38]. The experimental thermal hard photon multiplicities measured for the ^{129}Xe +
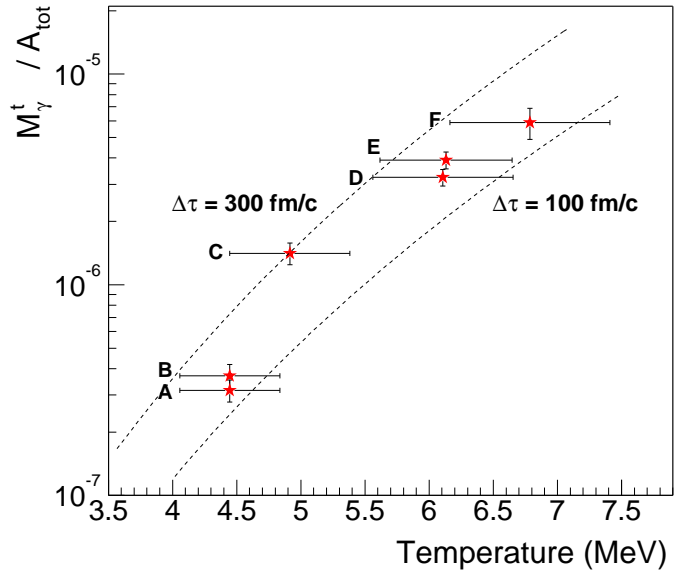

Fig. 8. *Thermal hard photon multiplicities, M_γ^t, divided by the total size of the system, $A_{tot} = A_t + A_p$, plotted as a function of the nuclear temperature extracted from Eq. 4, for the different $^{129}Xe + {}^{nat}Sn$ centrality classes. The lines correspond to two different values of source lifetime computed with Eq. 7.*

^{nat}Sn centrality classes exhibit a trend compatible with lifetimes of the order of 100-300 fm/c (Fig.8). In our measurements, within the data uncertainty, we do not observe any change of the lifetime of the equilibrated fragment with the impact parameter of the collision for Xe+Sn. The relatively large lifetime values obtained, jointly with the measurement of an important production of thermal hard photons, suggest that, at least for the investigated Xe+Sn reactions, the fireball does not undergo an instantaneous breakup from a rapidly expanding state (spinodal decomposition).

6.3 Caloric curve constructed from Xe + Sn exclusive measurements

As done in a previous paper for inclusive thermal photon measurements [12], we have measured the relationship between the estimated temperature and the excitation energy, $\epsilon^\star$, of the hot equilibrated fragment formed in Xe + Sn reactions at the different centralities studied in this work. At variance with experiments that measure the excitation energy with charged particle detectors, we cannot determine "calorimetrically" $\epsilon^\star$ from our data. The excitation energy of Xe quasiprojectiles produced from peripheral to central collisions has been deduced by Steckmeyer *et al.* [18] as a function of the charged particle multiplicity measured by the INDRA detector. The methods described in [18] are based on the determination of the

velocity of the quasiprojectile. The excitation energy is calculated from the kinetic energies of products belonging to the source. We have employed the geometric method of Cavata *et al.* [29] to relate the average impact parameter of each Xe + Sn reaction class with the corresponding value of M_{cp}^{INDRA}, in order to obtain the measured value of $\epsilon^{\star}$ for each centrality class. The estimated M_{cp}^{INDRA} and $\epsilon^{\star}$ values are reported in Table 7.

Table 7. *Values of the charged particle multiplicity measured with INDRA, M_{cp}^{INDRA}, and of the estimated excitation energy, $\epsilon^{\star}$, for each Xe+Sn centrality class with averaged impact parameter $\langle b \rangle$.*

Centrality class	$\langle b \rangle$ (fm)	M_{cp}^{INDRA}	$\epsilon^{\star}(A$ MeV$)$
Inclusive	3.8 ± 1.0	25 ± 1	5.6 ± 1.0
A or Peripheral	7.6 ± 0.3	14 ± 1	2.8 ± 0.3
B	7.2 ± 0.3	16 ± 1	3.3 ± 0.4
C	4.2 ± 0.4	24 ± 1	5.2 ± 0.6
D	2.8 ± 0.4	27 ± 1	6.1 ± 0.7
E	2.2 ± 0.6	$29 ^{+2}_{-1}$	6.7 ± 0.7
F or Central	1.0 ± 0.9	$32 ^{+5}_{-2}$	$7.7 ^{+1.4}_{-1.0}(8.7 \pm 1.5)$

Fig. 9. *Caloric curve constructed from the thermal hard photon slope measurements for the $^{129}Xe + {}^{nat}Sn$ reaction at 50A MeV (Table 6) and the estimated excitation energies (Table 7), compared to the Fermi liquid model curves with inverse level-density parameters $K=8/A$ MeV (dashed line) and $K=13/A$ MeV (dotted line).*

The errors of $\epsilon^{\star}$ take into account the uncertainty of $\langle b \rangle$ and a $\sim$10% systematic error due to the reconstruction of the quasiprojectile [18]. As expected, the excitation energy decreases linearly with increasing impact parameter. Since the highest measured charged particle multiplicity does not correspond to a real $\langle b \rangle = 0$, the geometrical method used to relate $\langle b \rangle$ and M_{cp}^{INDRA} is not accurate enough for central collisions. We therefore also quote in parentheses for centrality class F the value of $\epsilon^{\star}$ predicted for central collisions by the model of Natowitz *et al.* [39]. The caloric curve obtained is displayed in Fig. 9. The temperature increases smoothly with the excitation energy, the $(\epsilon^{\star},T)$ pairs obtained are below the expected Fermi fluid curves $(T = \sqrt{K\epsilon^{\star}}$ (MeV) with K = 8/A – 13/A MeV covering the known range of average nuclear level density parameters [40]). Peripheral reactions (classes A and B) lead to excitation energies $\epsilon^{\star} \approx 3A$ MeV, near those identified as the onset of the leveling region of the caloric curve for nuclear systems of size A= 180–241 [4].

7 Summary

Hard photon ($E_{\gamma} > 30$ MeV) emission has been studied in ^{129}Xe + ^{nat}Sn at 50A MeV for six bins of impact-parameter. The thermal component has been determined from a double source analysis of the measured spectra. For each centrality class, the temperature of the produced nuclear systems has been extracted from the measured thermal hard photon slope, by applying a thermal nuclear bremsstrahlung model that successfully reproduces the measured thermal hard photon spectral shape and multiplicities. The temperature obtained exhibits a small
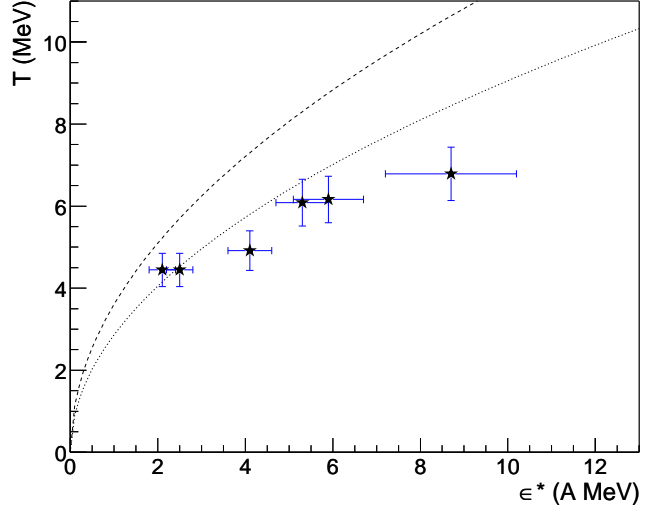
but systematic increase with decreasing impact parameter, from $T = 4.4$ MeV for the most peripheral collisions ($b/b_{max} \approx 0.6$) to $T = 6.8$ MeV for the most central class ($b/b_{max} \leq 0.1$). The amount of second-chance bremsstrahlung emission measured in each centrality bin is well described by the thermal model by assuming emission times of the order $\tau \approx 100 – 300$ fm/c for all centralities. The lifetimes of the produced equilibrated sources have also been estimated for six other heavy-ion reactions for which thermal bremsstrahlung emission has been measured by the TAPS Collaboration. The inclusive thermal hard photon multiplicities measured as a function of the temperature T for the different reactions suggest lifetimes $\tau \sim 100$ fm/c, i.e. between two and three times longer than the transit time of the colliding ions at these energies. Such relatively large time scale disfavor scenarios of instantaneous spinodal break-up and is more consistent with sequential fragmentation from a thermally equilibrated source. It is worth noting, however, that for the two smallest target-projectile combinations, ^{86}Kr+^{58}Ni and ^{36}Ar+^{58}Ni at 60A MeV, which are the systems with more energy available in the nucleus-nucleus center-of-mass, the experimental thermal photon multiplicities seem to be better reproduced with shorter lived equilibrated sources ($\tau \sim 35$ fm/c).

Finally, we present for the first time a caloric curve, $\epsilon^{\star}(T)$, obtained from thermal hard photon measurements for different impact parameter bins of the same reaction, Xe + Sn. Such a curve falls below the one expected for a Fermi liquid, in agreement with the curve constructed from thermal hard photon slopes measured in different

heavy-ion reactions [12], and consistent also with the available systematics of nuclear caloric curves [4].

References

1. J. P. Bondorf, A.S. Botvina, A.S. Ilinov, I.N. Mishustin and K. Sneppen, Phys. Rept. **257** (1995) 133; L.G. Moretto and G.J. Wozniak, Ann. Rev. Nucl. Part. Sci. **43** (1993) 379.
2. V. E. Viola, Nucl. Phys. A **734** (2004) 487.
3. J. Pochodzalla *et al.,* Phys. Rev. Lett. **75**, 1040 (1995).
4. J. B. Natowitz, Phys. Rev. **C65**, 034618 (2002).
5. J. B. Natowitz *et al.,* Phys. Rev. Lett. **89**, 212701 (2002).
6. W. Trautmann, nucl-ex/0411023, Proceedings INPC2004, Goeteborg, Sweden, June 27-July 2 (2004).
7. H. Nifenecker and J. Pinston, Ann. Rev. Nucl. Part. Sci. **40**, 113 (1990).
8. G. Martínez *et al.,* Phys. Lett. **B349**, 23 (1995).
9. Y. Schutz *et al.,* Nucl. Phys. **A622**, 404 (1997).
10. D. d'Enterria *et al.,* Phys. Rev. Lett. **87**, 22701 (2001).
11. D. Neuhauser and S.E. Koonin, Nucl. Phys. **A462**, 163 (1987).
12. D. d'Enterria *et al.,* Phys. Lett. **B538**, 27 (2002).
13. M.J. van Goethem *et al.,* Phys. Rev. Lett. **88**, 122302 (2002).
14. N. Marie Phys. Lett. **B391**, 15 (1997).
15. N. Marie *et al.,* Phys. Rev. **C58**, 256 (1999).
16. D. Gourio *et al.,* Eur. Phys. J. **A7**, 245 (2000).
17. N. Bellaize *et al.,* Nucl. Phys. **A709**, 367 (2002).
18. J.C. Steckmeyer *et al.,* Nucl. Phys. **A686**, 537 (2001).
19. R. Novotny, IEEE Trans. Nucl. Sci. **38**, 379 (1991).
20. M. Laval *et al.,* Nucl. Inst. and Meth. **A206**, 69 (1983).
21. A. Gabler *et al.,* Nucl. Inst. and Meth. **A346**, 164 (1994).
22. D.W. Stracener *et al.,* Nucl. Inst. and Meth. **294**, 485 (1990).
23. S. Luke *et al.,* Phys. Rev. **C47**, 1211 (1993).
24. R. Ortega, Ph.D.Thesis, Univ. Aut. de Barcelona, 2003.
25. L. Tassan-Got, Nucl. Inst. Meth. **B194**, 503 (2002).
26. J. van Pol, Ph.D.Thesis, Rijkuniversiteit Groningen, 1995.
27. R. Ortega, F. Fernández, D. D'Enterria and G. Martínez, Acta Phys. Polon. B **33**, 965 (2002).
28. H. Nifenecker and J.P. Bondorf Nucl. Phys. **A442**, 478 (1985).
29. C. Cavata *et al.,* Phys. Rev. **C294**, 47 (1993).
30. S. Riess *et al.,* Phys. Rev. Lett. **69**, 1504 (1992).
31. G. Martínez *et al.,* Phys. Lett. **B334**, 23 (1994).
32. J.J. Gaardhoje *et al.,* Phys. Rev. Lett. **59**, 1409 (1987).
33. J.H. Le Faou *et al.,* Phys. Rev. Lett. **74**, 3321 (1994).
34. T. Suomijärvi *et al.,* Phys. Rev. **C53**, 2258 (1996).
35. B.L. Berman and S.C. Fultz, Rev. Mod. Phys. **47**, 713 (1975).
36. R. Wada *et al.,* Phys. Rev. **C69**, 044610 (2004).
37. L. Beaulieu *et al.,* Phys. Rev. **C84**, 5974 (2000).
38. Z. He *et al.,* Phys. Rev.**C63**, 011601 (2001).
39. J.B. Natowitz *et al.,* Z. Phys. **A325**, 467 (1986).
40. B. Nerlo-Pomorska *et al*, Int. J. Mod. Phys. E **14** (2005) 505